Adsorptive and photocatalytic remediation of aqueous organic dyes and chromium(VI) by manganese(II) substituted magnetite nanoparticles

P. Mahapatra, S.K. Giri, N. Das*

Department of Chemistry, Utkal University, Bhubaneswar 751 004, India, Tel. +91-0674 2567734, email: dasnn64@rediffmail.com (N. Das)

ABSTRACT

A series of Mn-substituted magnetite nanoparticles (MN-MNPs), $Mn_xFe_{3-x}O_4$ ($0.0 \leq x \leq 0.63$), were synthesized by coprecipitation method and their structural, magnetic, and optical behaviours as a function of Mn^{2+} substitution were investigated by powder XRD, FT-IR, SEM-EDX, TEM, UV-Vis DRS, and magnetic moment measurements. XRD showed single-phase spinel structure for all the samples with an average crystallite sizes in the range 12.1–14.5 nm which were in good agreement with TEM results. The values of saturation magnetization (σ_s) were increased with increase of Mn content up to $x \leq 0.205$ and then decreased on further increase of Mn content. The catalytic activities of Mn-MNPs were evaluated with photo-decolourisation of different organic dyes (Methyl orange, Congo red and Rhodamine B) and photo-reduction of Cr(VI) under visible light irradiation. Among all, $Mn_{0.205}Fe_{2.795}O_4$ (Mn-MNP-3) showed the best performance with $\geq 85\%$ decolourisation of dyes (20 mg/L) within 4 h. Aqueous Cr(VI) was efficiently reduced by Mn-MNP-3; the rate and percentage of Cr(VI) reduction was enhanced by addition of different sacrificial agents. Photo-reduction of Cr(VI) was also improved in binary component system with a dye (Congo red) showing synergetic effect between the reduction and oxidation reactions. Simultaneous decontamination of Cr(VI) and a dye by the present catalytic system with easiness of separation may be useful in treatment of textile wastewater containing dye and heavy metals like Cr(VI).

Keywords: Mn-substituted magnetite; Magnetic nanoparticles; Nanophotocatalyst; Dye degradation; Cr(VI) photoreduction

1. Introduction

Water pollution caused by industrial effluents containing organic dyes and/or heavy metals continues to be a major environmental concern across the globe. Due to large scale production and extensive use in industries like textile, paper, carpet, leather, distillery, printing etc., organic dyes have become a significant part of industrial wastewaters [1–3]. Discharge of large volume of these wastewaters into the fresh water bodies not only damage the aesthetic nature of the aquatic environment but also affects the water transparency, resulting reduction of sunlight penetration, gas solubility and the photosynthetic reaction. Many of these dyes have been identified as toxic and even carcinogenic to mammals. Due to complex aromatic molecular structure and recalcitrant nature, most of the synthetic organic dyes are stable to light/oxidation and possess poor biodegradability and decolourisation. Hence, these colour bearing industrial effluents need to be treated efficiently and economically to bring down the concentration of hazardous dye within permissible limit before their discharge into the fresh water bodies to protect the aquatic and terrestrial environments, public health, and well-being [3–5].

The coexistence of heavy metal ions in textile effluents is a common phenomenon [6]. Heavy metals like as Cu, Co, and Cr are used as reducing agents/dye bath additives in dye fixation and form stable complexes which are resistant to decomposition. Among heavy metals, chromium in its

*Corresponding author.

hexavalent form (Cr^{VI}) is highly toxic to human, animals, plants, and microorganisms inhabiting in aquatic environments [7]. Besides textile production industries, chromium also enters into the aquatic environment through discharge of effluents from leather tanning, metal finishing, chrome plating, paint manufacturing units and electroplating industries. Due to acute toxicity, Cr(VI) has been put on the top-priority list of toxic pollutants by many countries. The World Health Organization (WHO) has set the maximum allowable limit for the discharge of Cr(VI) into inland surface waters and drinking water supplies as 0.10 and 0.05 mg/L, respectively [8].

During the past two-three decades, several conventional and advanced oxidation based techniques have been reported for removal of organic dyes and heavy metals from wastewaters and a few of them have been practically viable/applied in real systems [3–5,9,10]. The co-existence of metal ions and dye in wastewaters can complicate conventional treatment processes as it requires to be treated separately. In that case, photocatalysis techniques may provide a viable alternative for simultaneous remediation of dyes and hexavalent chromium. Simultaneous photocatalytic removal of organics as well as inorganic metal pollutants from wastewaters without addition of extra chemicals has a great practical importance in the field of pollution control and remediation [11]. Semiconductor based oxides materials have been extensively explored for photocatalytic degradation/reduction of dye molecules or Cr(VI) in single component systems [12–15]. In comparison, simultaneous photocatalytic remediation of organic dyes and Cr(VI) using oxide based photocatalytic system [16–19] or bacterial species [20,21] have been sparsely studied. As such there is a quest to develop efficient catalytic systems capable of working under visible/solar light for simultaneous photocatalytic removal of hazardous components from water and real-world implementation. Use of magnetic photocatalytic systems provides added advantage of separating the catalyst after the photocatalytic process for reuse. In this regard, use of magnetic nanophotocatalysts with relatively low band gaps (≤ 2.0 eV) could be a viable option in terms of activity under visible/sunlight as well as easy separation of catalysts from the reactant solution by an external magnetic field for repeated use.

Magnetite (Fe_3O_4) and substituted magnetites are well known inverse spinel structured ferrites and have gained significant scientific and technological interest. Their high biocompatibility and favourable magnetic/optical properties lead to many potential applications in the fields of data storage, ferrofluids, MRI, biomedicine, biosensor, bio-separation, magnetic nano-adsorbents and catalysis [22–25]. The optical, structural and magnetic properties can be further modified by replacing certain degree of Fe(II) ions with different metal ions like Co, Zn, Ni and Mn without disturbing the spinel structure [23–28]. Introduction of transition metal cations with variable oxidation states like Mn and Co in the spinel lattice has modified the microstructure as well redox behaviour of the magnetite; an important factor in catalysed oxidation/reduction reactions [27–29].

Adsorptive and/or photocatalytic removal of different organic and inorganic contaminants from wastewaters using magnetic nanomaterials has generated great interest in recent years owing to their faster adsorption,

higher adsorption capacity, photocatalytic activity under visible light and easy separation by application of external magnet [30–32]. The efficiency of magnetite nanoparticles towards adsorptive/photocatalytic removal of organic dyes or Cr(VI) have been demonstrated in several studies but the effect of transition metal substitution has been sparsely studied [30–34]. In view of above, a series of Mn(II) substituted monocrystalline magnetite ($Mn_xFe_{3-x}O_4$; $x = 0.00$–0.63) were prepared by coprecipitation and characterised by various physicochemical methods. The adsorption/photocatalytic efficiency towards remediation of several organic dyes and Cr(VI), alone and in combination, were also evaluated to see effect of Mn(II) substitution and understand the overall photocatalytic process in a binary-contaminants system.

2. Experimental

2.1. Materials

$FeCl_3$ (anhydrous), $FeCl_2 \cdot 4H_2O$, $MnCl_2 \cdot 4H_2O$ and liquid ammonia (GR, Mecrk) were used in synthesis of materials. Methyl orange (MO), Congo red (CR), Rhodamine B (RhB) and potassium dichromate, as procured from Merck (India), were used in photocatalytic runs. All other chemicals used were of GR/AR grade and deionized distilled water was used in all experiments.

2.2. Synthesis of magnetite and Mn(II) substituted magnetite nanoparticles

All the samples were prepared by coprecipitation under supersaturating condition of hydroxide ion concentration in N_2 atmosphere. $FeCl_3$, $FeCl_2 \cdot 4H_2O$ and $MnCl_2 \cdot 4H_2O$, in desired stoichiometric ratio, was dissolved in minimum volume of dilute HCl. The acidic solution was then added dropwise to a well stirred aqueous solution of NaOH (1.5 M), taken in a two naked round bottom flask. At the end of addition, the temperature of flask was raised to 80°C and the whole mass was stirred at this temperature for 1 h. After cooling to room temperature, the black precipitate of Fe_3O_4 or Mn substituted Fe_3O_4 was magnetically separated from the precipitating agents, washed successively with oxygen free distilled water and acetone for three times and finally dried at 50°C under vacuum. The dried samples were preserved in air-tight bottles for characterisations and adsorption/photocatalytic studies. All together five Mn substituted Fe_3O_4 samples were prepared with fixed Fe^{3+}: ($Fe^{2+} + Mn^{2+}$) molar ratio (2:1) and varying the Mn^{2+} molar concentration for partial replacement of Fe^{2+}. The samples were denoted as Mn-MNP-x ($x = 0$–5) depending on the amount of Mn substitution.

2.3. Characterisations

The total Fe, Fe(II) and Mn(II) contents in different samples were determined by conventional wet chemical and AAS analyses [34]. X-ray diffraction (XRD) measurements were recorded on a Rigaku Miniflex II X-ray diffractometer equipped with Ni filtered CuK_α (30 kV, 15 mA) radiation source with a scan speed of 1°/min and a step

size of 0.02°. The average crystallite size was estimated from broadening of the main diffraction peaks, using Debye-Scherrer formula:

$$D = 0.9\lambda/\beta \cos\theta \tag{1}$$

where D is the average crystallite size, λ is the X-ray wavelength equal to 1.5406 Å, β is the full width at half maximum (FWHM) and θ is diffraction angle. FT-IR spectra in KBr phase were recorded using a Shimadzu IR Affinity 1 FT-IR with a nominal resolution of 4 cm^{-1} and averaging 100 scans to improve signal to noise ratio. The UV-Visible diffuse reflectance (UV-Vis-DR) spectra were recorded on a Shimadzu 2550 UV-Visible spectrophotometer using $BaSO_4$ white reference and used to calculate the optical energy band gap (E_g) values as per theory established by Kubelka-Munk. Particle size distribution and morphology of selected samples were investigated transmission electron microscope (FEI, TECHNI, B^2 20, SEM TWIN) operated at 200 kV. Scanning electron micrographs of selected sample before and after adsorption/decolourisation of dye (Congo red) were performed using Zeiss Gemini SEM 300 coupled with energy-dispersive X-ray spectroscopy (EDX). Saturation magnetization was measured by a SQUID-vibrating sample magnetometer (VSM) at room temperature. The BET surface area of samples were measured using Smart Sorb 92/93 surface area analyser after degassing the samples under vacuum (2×10^{-4} Pa) at 100°C. The point of zero charge (pH$_{pzc}$) was determined by potentiometric acid-base titration method [34].

2.4. Photocatalytic dye decolourisation and/or Cr(VI) reduction experiments

The Photocatalytic activity of different samples was evaluated for decolourisation of three commonly used organic dyes (MO, CR and RhB) and reduction of Cr(VI) under visible light (VL) except otherwise mentioned. Experiments were carried in a double walled glass reactor with an effective volume 100 ml. A 125 W high pressure Hg lamp, fitted to the reactor, provided the light source. The lamp was equipped with a cutoff filter to remove any radiation < 420 nm and to ensure irradiation only by visible light. All the experiments were performed under stirring condition in ambient air and at constant temperature (30.0±0.2°C).

Typically, a weighed amount of catalyst was dispersed in 100 ml aqueous solution of dye and the pH was adjusted to the desired value (±0.02) by adding NaOH/HCl (0.01 M) solutions. The reactant solution was irradiated with visible light under stirring condition. At regular intervals or at the end of reaction, a definite portion (3–5 ml) of reactant solution was withdrawn and magnetically separated the solid catalyst. The concentration of residual dye in the supernatant was computed from the absorbance values measured at fixed wavelengths i.e. 545, 455 and 554 for MO, CR and RhB, respectively. Further variations of reaction parameters were carried out using the sample showing the highest activity. For Cr(VI) photoreduction, an aqueous solution of Cr(VI) at desired concentration and pH was irradiated with visible light. The residual concentration of Cr(VI) in the reactant solution, after separation of catalyst, was estimated using diphenyl-carbazide method by measuring the absorbance

values at 540 nm. The efficiency of dye decolourisation or Cr(VI) reduction was evaluated using Eq. (2).

$$\text{Dye decolourisation/Cr(VI) reduction (\%)} = (C_0 - C_t)/C_0 \times 100 \tag{2}$$

where C_0 and C_t are the concentrations of dye or Cr(VI) at the beginning and at time 't', respectively. A few photocatalytic runs were also carried out under direct sunlight (SL) in between 10.00 am to 3.00 pm during summer in Bhubaneswar city (20.27 latitude and 85.83 longitude), India when the average intensity of light was 7.5×10^4 lx (Lutron LX 1102 Digital Light Meter). In order to see the adsorption behaviour of Mn-substituted Fe_3O_4 samples towards dyes/Cr(VI), experiments were carried out under identical conditions of photocatalytic runs but without visible light irradiation. Control experiments without catalyst were also carried out to see the photolysis of dye and Cr(VI).

3. Results and discussion

3.1. Characterisations of sample

The compositions of solid samples (Table 1), derived from chemical analyses, closely match with the Fe^{3+}: Fe^{2+}: Mn^{2+} molar ratios taken in solution for synthesis. Powder XRD patterns of as synthesised samples are given in Fig. 1. All the patterns match well with a single-phase cubic spinel structure and the main peaks are consistent with those of standard cubic Fe_3O_4 (JCPDS no. 19-629). The relatively low intensity and broad peaks further indicate small crystallite size of the sample particles. The average crystallite sizes of different samples, calculated by Debye-Scerer's formula using diffraction width of (311) peak, are found in the range 12.15 to 14.35 nm (Table 1). As evident from the table, the crystallite size of $Mn_xFe_{3-x}O_4$ particles decreases at lower level of Mn^{2+} substitution and then increases marginally with further increase of Mn^{2+} content. Decrease of crystallite size with increasing Mn content has been reported previously [27–29] while Saravanan et al. reported a reverse trend with increase of Mn content [26].

The morphology was investigated by taking SEM and TEM of some selected samples. SEM images of Mn-MNP-3 with EDX are presented in Fig. S1. The EDX spectrum of Mn-MNP-3 confirms the presence of Fe and Mn in molar

Table 1
Chemical composition and physicochemical properties of as synthesized $Mn_xFe_{3-x}O_4$ samples

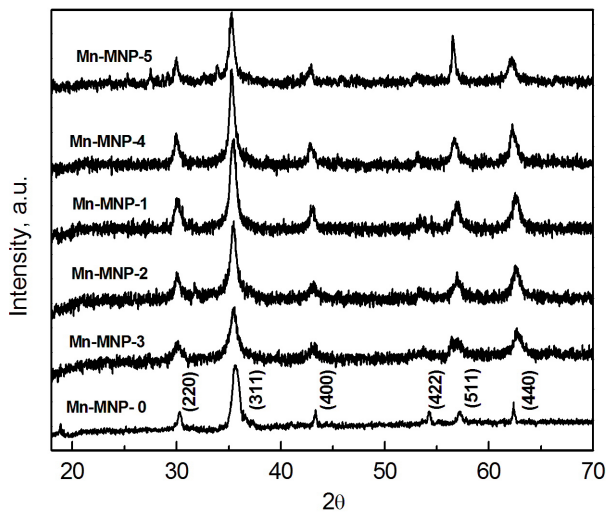| Sample code	Value of x in $Mn_x Fe_{3-x}O_4$	Mean crystalline size, nm	Surface area, m^2/g	Band gap, eV
Mn-MNP-0	0.00	13.83	33.4	1.65
Mn-MNP-1	0.054	13.09	32.9	1.67
Mn-MNP-2	0.126	13.02	31.1	1.62
Mn-MNP-3	0.204	12.15	31.8	1.61
Mn-MNP-4	0.412	14.02	29.4	1.57
Mn-MNP-5	0.630	14.58	27.2	1.53

Fig. 1. XRD patterns of Fe_3O_4 and Mn-substituted Fe_3O_4 nanoparticles.

proportion close to that obtained from chemical analysis. The SEM images (Figs. S1a, b) show aggregates of magnetic nanoparticles within few microns presumably due to effect of magneto dipoles and van der Wall forces. After adsorption/photodecolouisation of CR, the SEM images shows smaller aggregates (Fig. S1c, d) with lower porosity due to partial adsorption of residual CR molecule and some degraded products after photocatalytic run. Figs. 2a–d display the TEM micrographs of as prepared Fe_3O_4 and Mn substituted-Fe_3O_4 (Mn-MNP-3) nanoparticles. As evident from the micrographs, the particles are mainly polyhedral in shape along with some aggregates. There is no distinctive change in morphology with the substitution of Mn. The average sizes of nanoparticles, observed in the TEM images, are in good agreement to the crystalline size estimated from Scherrer formula in XRD pattern. Selected area electron diffraction (SAED), performed on isolated nanocrystals, exhibits five rings attributing to (220), (311), (400), (511) and (440) reflections of crystalline magnetite, respectively [35].

Room temperature magnetization curves of neat and Mn-substituted Fe_3O_4 nanoparticles with varying externally applied magnetic field (±20 kOe) are shown in Fig. 3. The

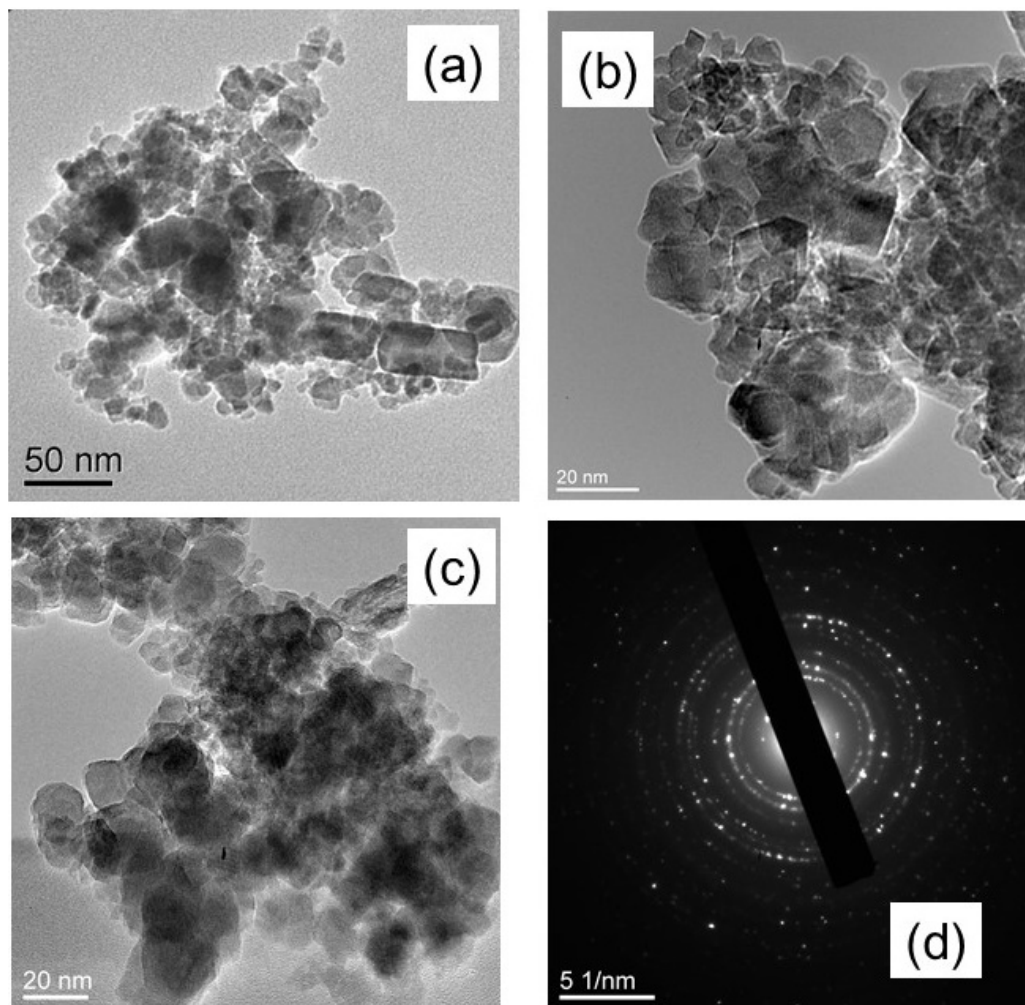Fig. 2. TEM micrographs of (a) Fe_3O_4; Mn-substituted (b) Mn-MNP-3 and (c) Mn-MNP-5 Fe_3O_4 nanocrystals; (d) SAED pattern of Mn-MNP-3.

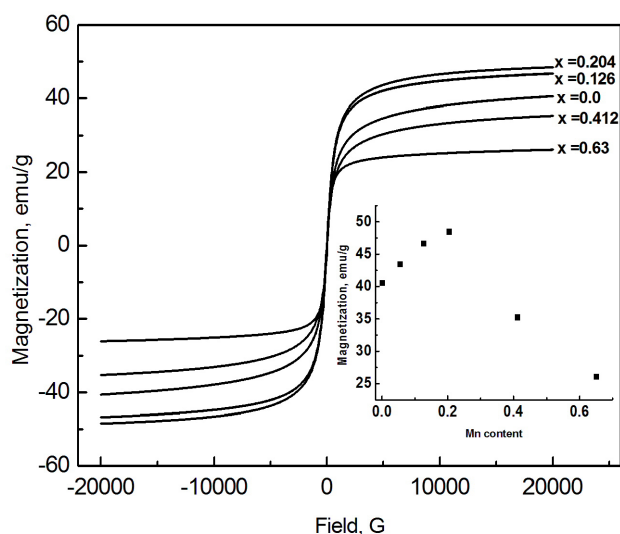Fig. 3. Magnetization curve of Fe_3O_4 and Mn-substituted Fe_3O_4 nanoparticles.

Fig. 4. UV-Vis diffuse reflectance spectra of Fe_3O_4 and Mn-substituted Fe_3O_4 nanoparticles.

measured values of saturation magnetization (σ_s) of Fe_3O_4 and Mn-substituted Fe_3O_4 are apparently ≥ 60% lower than that of corresponding bulk magnetite (σ_s = 92 emu g^{-1}) and are very similar to the reported values [23–26,28]. The lowering of magnetization in nanoparticles is primarily due to one or more factors like effect of more antiferromagnetic exchange interactions, disordered cation distribution and formation of a magnetically dead surface layer. On substitution of Mn^{2+}, there is a steady increase of σ_s values with increase of Mn content at lower level ($x \leq 0.205$) but tends to decrease on further increase of Mn^{2+} content. The initial increase of σ_s values with lower Mn^{2+} content and decrease at higher Mn^{2+} content could be attributed to the resultant of sub-lattice magnetic moments [23–26].

UV-Visible-DR spectra of neat and selected Mn-substituted Fe_3O_4 nanoparticles are shown in Fig. 4. All the samples show significant absorption well extend in the visible region indicating higher photoactivity for the target reactions under visible light irradiation. Optical energy band gap (E_g) values, obtained from the extrapolated intercept of Tauc's plots, are given in Table 1. As evident, the E_g values of neat and Mn-substituted Fe_3O_4 nanoparticles are significantly less than the value reported for bulk magnetite (~0.1 eV) [34]. The E_g values are marginally decreased with the increasing Mn content. The FT-IR spectra of as prepared Mn-substituted Fe_3O_4 nanoparticles (Mn-MNP-3) and CR dye adsorbed Mn-MNP-3 before and after visible light irradiation (Fig. S2) show broad absorption band centered around 3400 cm^{-1} attributing to stretching mode of H_2O (n_{OH}) while relatively less intense bands around 1600 cm^{-1} correspond to the deformation mode (d_{H-OH}) [34]. The observed band at ~576 cm^{-1} in all the cases is attributed to Fe-O bonds vibrations. The FT-IR spectra of CR adsorbed Mn-MNP-3 shows several additional peaks characteristic of CR dye. Peaks at 1126 cm^{-1} for RSO_3^- stretching, 1590 cm^{-1} for the N=N stretching, 1447 cm^{-1} for the C=C stretching of aromatic compound, 3460 cm^{-1} for N–H stretching of primary amine and 1335 cm^{-1} for the C–N bending clearly indicate the adsorption of CR. After photocatalytic run,
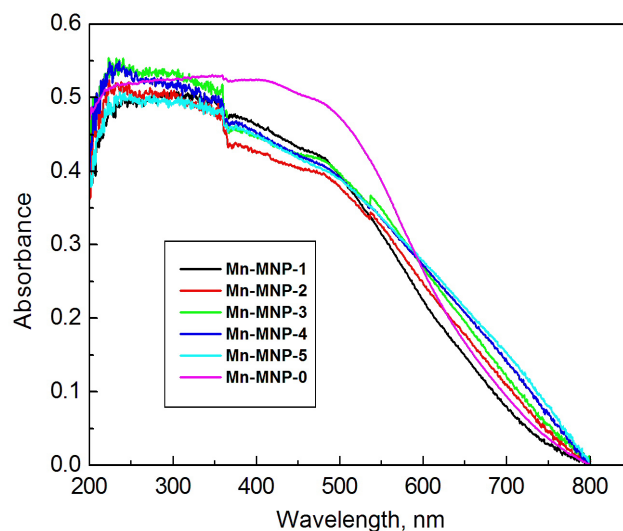
the intensities of all CR peaks are greatly reduced indicating degradation of CR into smaller molecules followed by desorption of these molecules from the catalyst surface.

The surface area values of all the samples are relatively low (28.8–33.4 m^2/g) and decrease with increase of Mn content (Table 1). The point of zero charge (pH$_{pzc}$) values, derived from acid-base titration curve are found in the range 7.6–6.9 with highest and lowest values shown by neat Fe_3O_4 and Mn substituted sample with highest Mn content, respectively. These are well within the range of values reported for similar materials [29,34].

3.2. Photocatalytic activity

3.2.1. Photodecolourisation of dyes

The time course UV-Visible spectra of different dyes (MO, CR, RhB) in the photocatalytic runs are presented in Figs. 5–7. Clearly, the main absorbance peaks of MO and CR decrease with time without any observable shift in the peak positions due to decolourisation of dyes. Further exposure with VL leads to no new absorption peak in the whole spectrum indicating the dye degraded products exhibit no different peaks. The decolourisation of RhB is also evident from the large decrease in absorbance change during the photocatalytic reaction and is mainly due to breaking of conjugated chromophore structure rather than de-ethylation of RhB [34]. It is also seen that the adsorption/photo-decolourisation during initial 60 min is relatively fast followed by slow decolourisation process up to 240 min, which is partly due to coverage of catalyst surface by the dye molecules/degraded products of dyes during the reaction. The extent of decolourisation of dyes by different samples, in presence and absence of visible light irradiation, are also presented in Figs. 5–7 (inset). As seen, the adsorption of all the dyes on different samples under dark condition is within 30%. The adsorption (%) progressively increases with increase of Mn content in the samples for anionic dyes (MO and CR) while the cationic (RhB) shows a marginal decreas-
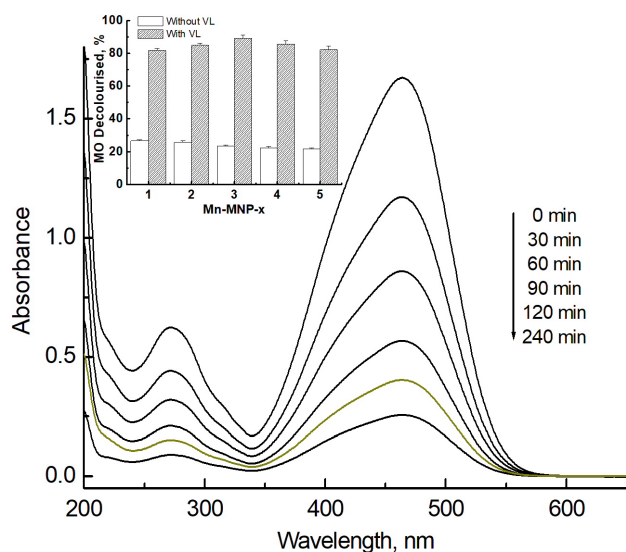
Fig. 5. Time course spectral scan of MO dye (10 mg/L) under visible light with Mn-MNP-3 (1.0 g/L). (Inset) Comparative adsorptive and photocatalytic decolourisation of MO by different Mn-MNPs (MO, 20 mg/L; Mn-MNPs, 1.0 g/L; pH, ~5.0, Reaction time, 4 h).

Fig. 6. Time course spectral scan of CR dye (10 mg/L) under visible light with Mn-MNP-3 (1.0 g/L). (Inset) Comparative adsorptive and photocatalytic decolourisation of CR by different Mn-MNPs (CR, 20 mg/L; Mn-MNPs, 1.0 g/L; pH, ~5.0, Reaction time, 4 h).
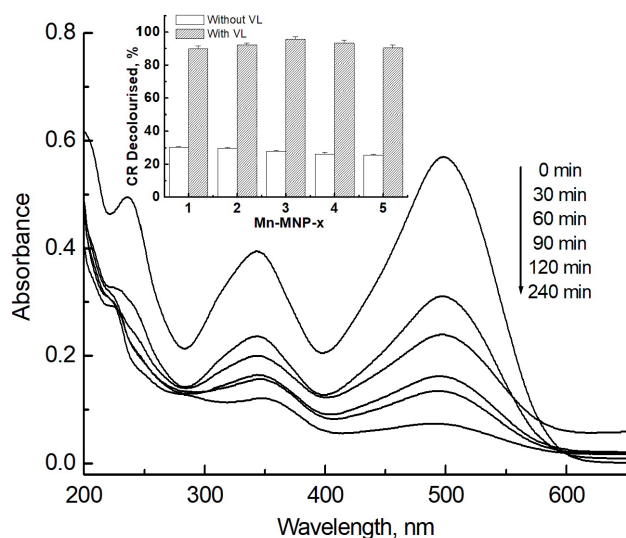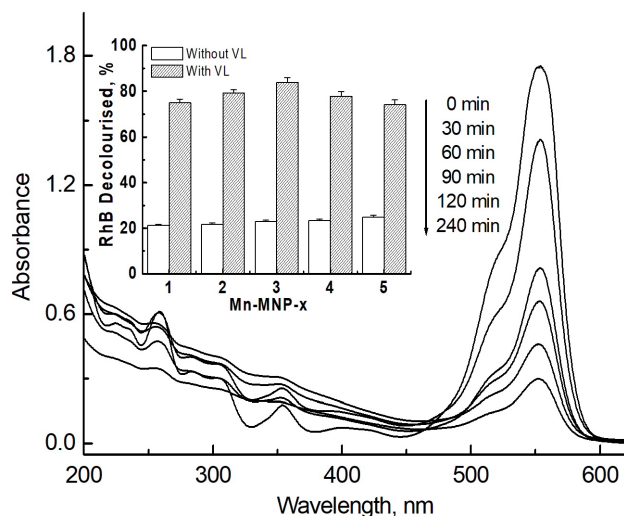

Fig. 7. Time course spectral scan of RhB (10 mg/L) under visible light with Mn-MNP-3 (1.0 g/L). (Inset) Comparative adsorptive and photocatalytic decolourisation of RhB by different Mn-MNPs (RhB, 20 mg/L; Mn-MNPs, 1.0 g/L; pH, ~5.0, Reaction time, 4 h).

ing trend with increase of Mn content. This observed trend of dye adsorption is attributed to the combined effects of decreased surface area and pzc values of Mn-MNP samples with increase of Mn content. Control experiments without catalyst showed that the decolourisation of all three dyes due to photolysis is less than 5% after 4 h of reaction. On addition of catalyst, the overall decolourisation of dyes is more than 75% indicating significant photocatalytic activity of Mn-MNP samples. As evident from Figs. 5–7 (inset), the

sample with intermediate Mn content (Mn-MNP-3) exhibits the highest photocatalytic activity which is mainly due to the effective charge separation between photogenerated (h^+/e^-) pair. The decreased photocatalytic activity at higher Mn content is presumably due to some structural changes such as introduction of defects which increases the (h^+/e^-) pair recombination and thereby reduction of photoactivity. Enhanced activity due to Mn substitution in magnetite samples has been reported for heterogeneous Fenton/photo-Fenton decolourisation of dyes [27,29]. Further variations of experimental parameters were carried out using the sample (Mn-MNP-3) showing the highest activity. In order to see photoactivity of Mn-MNP-3 under sunlight, photo-decolourisation of dyes were carried under similar set of conditions as that of visible light irradiation. It is seen that the photo-decolourisation activity of Mn-MNP-3 under visible light irradiation is significantly higher than that under sunlight. For instance, the percent decolourisation of MO, CR and RhB (20 mg/L each) under sunlight are 45, 50 and 43%, respectively as against 89.1, 95.7 and 83.9% under visible light irradiation.

The pH of aqueous dye solution significantly affects the overall adsorption/photocatalytic decolourisation of a dye by oxide based photocatalysts, primarily due to the variation of surface charge of the photocatalysts and degree of ionization of the dye molecule with change of pH. In order to avoid any colour change owing to later factor with pH variation that leads to change in the absorbance values, the pH of the dye solution was kept at pH ≥ 5; above the acid dissociation constant (pK_a) of dyes (MO, 4.2; CR, 3.5–5.0 and RhB, 3.7) where the dyes mostly exist in dissociated/zwitterionic forms.
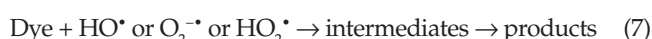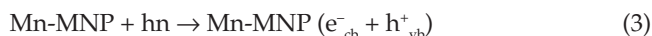
In order to see the effects of amount of photocatalyst and dye concentration, the experiments were carried out by varying the amounts of photocatalyst (0.25–2.0 g/L) and initial dye concentration (10–50 mg/L) keeping the

other parameters constant. It is seen that the overall decolourisation of all three dyes increased non-linearly, especially with catalyst does ≥ 1.5 g/L, with increase of catalyst dose. This is primarily attributed to the increased number of adsorption and active sites on the catalyst surface. On variation of catalyst dose from 0.25 to 2.0 g/l, the percent decolourisation of MO, CR and RhB (50 mg/L) increased from 15.4 to 60.3, 18.3 to 66.1 and 10.4 to 50.3, respectively. Non-linear increase of decolourisation at higher dose (≥1.5 g/L) is mainly attributed to the increased opacity of the suspension that reduces the light penetration and thereby photoactivated volume of the suspension. Also aggregation of catalyst particles at higher dose is more likely causing decrease of number of active sites. On the other hand, the percent decolourisation of MO, CR and RhB decreased progressively with increase of initial dye concentrations from 10 to 50 mg/L. Decrease of dye decolourisation is more pronounced at higher concentration partly due to adsorption of some degradation intermediates upon catalyst surface. Nearly complete decolourisation of all three dyes with initial dye concentration 10 mg/L and catalyst (Mn-MNP-3) dose 1.0 g/L was achieved in 4 h of irradiation. The photocatalytic efficiencies of some iron based oxides/ferrites photocatalysts along with current catalytic system are presented in Table 2 [33,36–40]. It is seen that the efficiency of the present catalytic system is comparable or better than the other iron based catalyst especially under visible light irradiation.

Based on the above results, the possible pathways of photocatalytic dye decolourisation under visible light irradiation is described in Eqs. (3)–(7). In heterogeneous photocatalytic degradation/decolourisation of dye using semiconducting materials irradiated with light energy greater than the band gap energy (E_g), as in the present case, photogeneration of electron–hole pair [Eq. (3)] is mainly responsible for the reaction. Photogenerated h^+ in the valence band reacts with either H_2O or OH^- to produce the $HO^\check{Y}$ through the reactions [Eqs. (4) and (5)] while e^- in the conduction band reacts with adsorbed O_2 on the catalyst surface to generate $O_2^{-\bullet}$ and subsequently generate $HO^\bullet$ in several steps [Eq. (6)]. Finally $HO^\bullet$ or $O_2^{-\bullet}$ or $HO_2^\bullet$ radicals react with dye molecules to yield the degraded products.

Excitation of surface-adsorbed dye molecule by absorption of photons of visible light followed by transition into the conduction band of the catalyst and subsequent oxidation of dye molecule cannot be neglected.

$$Mn\text{-}MNP + hn \rightarrow Mn\text{-}MNP\ (e^-_{cb} + h^+_{vb}) \tag{3}$$

$$H_2O + h^+_{vb} \rightarrow H^+ + OH^{\check{Y}} \tag{4}$$

$$HO^- + h^+_{cb} \rightarrow HO^{\check{Y}} \tag{5}$$

$$e^-_{cb} + O_2 \rightarrow O_2^{-\bullet} \rightarrow\ HO_2^\bullet \rightarrow HO^\bullet + OH^- + O_2 \tag{6}$$

$$Dye + HO^\bullet\ or\ O_2^{-\bullet}\ or\ HO_2^\bullet \rightarrow intermediates \rightarrow products \tag{7}$$

3.2.2. Adsorption and photoreduction of Cr(VI) by Mn-MNP samples

Iron based magnetic nanoparticles are well known as adsorbent and photoreductant for a variety of inorganic water contaminants which exist in the anionic forms like hexavalent chromium [7,13,18]. In order to assess the efficiency of present catalytic system, Cr(VI) adsorption/photoreduction experiments were carried out under visible light irradiation using Mn-MNP-3 sample showing highest activity in dye decolourisation. For all adsorption experiments, the pH and initial Cr(VI) concentration were varied keeping the amount of Mn-MNP-3 (1.0 g/L) and time of adsorption (4.0 h), maximum time required for attaining the adsorption equilibrium, fixed.

The influence of solution pH on Cr(VI) adsorption is illustrated in Fig. 8 (inset), which shows the adsorption is highly pH dependent. It is seen that the percentage of Cr(VI) adsorption decreases gradually as the solution pH increases from 3.0 to 8.0 and the uptake of Cr(VI) by Mn-MNP-3 also decreases from 9.96 to 3.4 mg/g. Higher adsorption of Cr(VI) at lower pH can be explained on the basis of electrostatic interaction. Initial solution pH controls not only the surface charge and degree of protonation of adsorbent but also the pH dependent speciation of the Cr(VI) ion. At

Table 2
Comparative photocatalytic activity of some iron based oxides/ferrites towards decolourisation aqueous organic dyes

| Catalytic system	Light Source	Dye	Reaction conditions				Conversion (%)	Ref
			[Dye], (mg/L)	pH	catalyst (g/L)	Time, (min)		
Fe_2O_3-Fe_3O_4	VL	MO	19.83	–	0.50	170	65.1	36
Fe_2O_3-Fe_3O_4/Clay	VL	MO	19.68	–	0.50	170	77.2	36
Fe_3O_4/ZnO/GO	VL	MO	3.27	–	0.20	120	92.8	37
Mn-MNP-3	VL	MO	20.0	5.0	1.0	240	89.2	This work
Fe_3O_4	UV	CR	69.6	4.0	0.20	60	55.2	38
Mn-MNP-3	VL	CR	20.0	5.0	1.0	240	95.8	This work
Mesoporous α-Fe_2O_3	UV	RhB	4.75	–	0.50	135	84.9	39
Fe_3O_4	VL	RhB	20.0	7.5	0.51	120	64.3	40
Fe_3O_4/rGO	SL	RhB	47.8	5.0	0.50	120	87.1	33
Mn-MNP-3	VL	RhB	20.0	5.0	1.0	240	83.9	This work
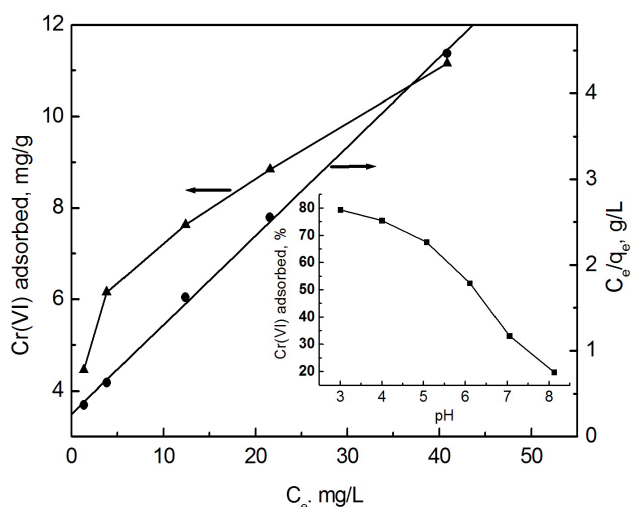
Fig. 8. Effect of initial concentration on Cr(VI) adsorption by Mn-MNP-3 and fitting of equilibrium adsorption data to Langmuir isotherm model. (Inset) Effect of pH on Cr(VI) adsorption.

pH > 6.5, CrO_4^{2-} species is predominant, while $HCrO_4^-$ and $Cr_2O_7^{2-}$ are prevalent at pH values ranging from 2.0 to 6.5. The surface positive charge and degree of protonation of Mn-MNP-3 decrease with increase of solution pH below its pH_{pzc} value (pH_{pzc} ~ 7.1) and results a decrease of Cr(VI) adsorption due to lowering of electrostatic attraction. At pH > 7.1, the surface charge of Mn-MNP-3 becomes negative which leads to an increase of electrostatic repulsion with Cr(VI) ions resulting a decrease of Cr(VI) adsorption . A similar trend for adsorptive removal of Cr(VI) by magnetite and ferrite nanoparticles has been reported in previous studies [41–44]. Although adsorption of Cr(VI) is highest at pH ~ 3.0 in the working pH range, subsequent adsorption/photoreduction experiments involving Cr(VI) were carried out at pH ~ 5.0 in order to maintain the uniformity with dye decolourisation experiments.

Cr(VI) removal efficiency was also studied as a function of initial concentration (5–50 mg/L) keeping the initial pH, Mn-MNP-3 dose and contact time constant. It is found that the adsorption of Cr(VI) decreases from 73 to 18.3% with the increase of the initial Cr(VI) concentrations from 5 to 50 mg/L. This may be attributed to the fact that the total adsorption sites available with the fixed dosage of Mn-MNP-3 are insufficient for Cr(VI) adsorption at higher concentrations. The equilibrium Cr(VI) adsorption data were further fitted to Langmuir and Freundlich isotherm models [Eqs. (8) and (9)].

$$C_e/q_e = 1\ /bq_m + C_e/q_m \qquad (8)$$

$$\ln q_e = \ln K_F + (1/n) \ln C_e \qquad (9)$$

where q_m (mg/g) is the maximum adsorption capacity corresponding to complete monolayer coverage and b (L/mg) is the Langmuir constant related with the adsorption energy. C_e (mg/L) and q_e (mg/g) are the concentration of Cr(VI) in the solution and the adsorption capacity at the equilibrium, respectively. K_F and n are Freundlich constants

with n giving an indication of the facility with which the adsorption process takes place. From the linear regression coefficient values (R^2), it is seen that the experimental data are well described by Langmuir isotherm (R^2 ~ 0.99) as compared to Freundlich (R^2 ~ 0.92). A comparison in terms of maximum adsorption capacity (q_m) of Mn-MNP-3 with other relevant adsorbents is shown in Table 3. As evident the value of q_m in the present case (10.1 mg/g) is relatively lower than those reported for magnetite or manganese ferrites samples [33,41–47]. The lower q_m value is primarily due to relatively higher solution pH (~5.0) maintained in the adsorption experiments than that used in the previous studies (pH ~ 2.0–3.0).

The phtoreduction of Cr(VI) were carried out at varying initial concentrations (5–20 mg/L) and the results obtained are presented in Table 4 and Fig. 9. The removal of Cr(VI) without light irradiation is mainly due to its adsorption on the catalyst surface. On irradiation with visible, the overall Cr(VI) removal is significantly increased at all concentrations (Fig. 9). It is also seen that the Cr(VI) reduction decreases with increase of initial Cr(VI) concentration due to availability of fewer active sites on the catalyst for photoreduction of Cr(VI) to Cr(III) (Table 4). The photoreduction efficiency of present catalytic system (Mn-MNP-3) is also compared with other relevant catalysts (Table 3). As seen in the table, the reduction efficiency of Mn-MNP-3 is found good considering the higher initial pH and concentration of Cr(VI) solution used in photoreduction experiments.

It is known that the photocatalytic reduction of Cr(VI) using semiconducting oxide catalysts is usually higher in the metal-organic-catalyst combination than in the single system (metal-catalyst) due to suppression of electron-hole recombination in presence organics which acts as a photo-generated hole scavenger or sacrificial agent (SA) [16–19,48]. In order to see the influence of organics, photoreduction of Cr(VI) (10–20 mg/L) was carried out in presence of different sacrificial agents (formic acid, phenol and EDTA) and the representative results are shown in Fig. 9. For a fixed amount (mg/L) of sacrificial agents, the photoreduction of Cr(VI) increases in the order EDTA ~ formic acid < phenol. However, in terms molar concentration of SA, the accelerating effect increases in the order formic acid < Phenol < EDTA. The observed trend is consistent with the reported results of Cr(VI) photoreduction in presence sacrificial agents using different photocatalysts [46,47]. In presence of sacrificial agents, the photoreduction rate of Cr(VI) also increases and requires less time than Cr(VI) alone. Both the percentage and rate of Cr(VI) photoreduction increase with increase of initial concentration of SA from 5 to 30 mg/L. Further increase of SA concentration (≥30 mg/L) results a decrease in the photoreduction presumably due to crossing the optimum SA concentration required for minimum electron-hole recombination.

Assuming adsorption of Cr(VI) is the first step in photoreduction process, a simple mechanism involving transfer of conduction band electrons from catalyst surface to adsorbed Cr(VI) is delineated in Eqs. (10)–(13) [33].
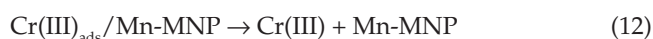
$$\text{Mn-MNP} + h\nu \rightarrow \text{Mn-MNP} (h^+/e^-) \qquad (10)$$

$$\text{Cr(VI)}_{ads}/\text{Mn-MNP} + 3\ e^- \rightarrow \text{Cr(III)}_{ads}/\text{Mn-MNP} \qquad (11)$$

$$\text{Cr(III)}_{ads}/\text{Mn-MNP} \rightarrow \text{Cr(III)} + \text{Mn-MNP} \qquad (12)$$
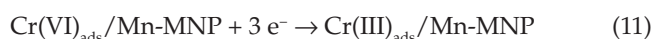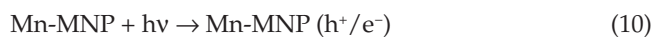
Table 3
Comparative activity of some selected relevant samples towards adsorption/photoreduction of aqueous Cr(VI)

| Catalytic system	Light source	Adsorption/Reaction conditions				Adsorption capacity (mg/g)	Photo reduction (%)	Ref
		[Cr(VI)] (mg/L)	pH	Catalyst (g/L)	Time (min)			
Synthesised Fe_3O_4	–	50	2.0–2.5	–	–	20.16	–	[41]
Commercial Fe_3O_4	–	50	2.0–2.5	–	–	13.72	–	[41]
$MnFe_2O_4$	–	50–250	2.0	1.50	120	89.2	–	[42]
$MnFe_2O_4$	–	100	3.0	5.0	60	19.6	–	[43]
$MnFe_2O_4$	–	100	–	2.0	60	17.5	–	[44]
Fe_3O_4 (Ti-residue)	–	10–50	5.0	3.0	1440	14.49	–	[45]
Fe_3O_4	–	100–400	5.5	2.0	60	121.9	–	[46]
Fe_3O_4	–	2 – 100	2.0	2.0	100	20.2	–	[47]
Mn-MNP-3	–	10–50	5.0	1.0	240	10.1	–	This work
Fe_3O_4/rGO	–	4.32	3.0	0.5	25	3.28	96.0	[33]
$MnFe_2O_4$	VL	15.0	2.0	1.0	60	–	82.0	[49]
$Zn_{0.2}Mn_{0.8}Fe_2O_4$	VL	15.0	2.0	1.0	60	–	85.0	[49]
$Cd_{0.2}Mn_{0.8}Fe_2O_4$	VL	15.0	2.0	1.0	60	–	92.0	[49]
TiO_2	UV	20.0	3.0	1.6	240	–	80.0	[50]
$NiFe_2O_4$-SiO_2-TiO_2	UV	20.0	3.0	1.6	300	–	60.0	[50]
Mn-MNP-3	VL	20.0	5.0	1.0	240	–	43.9	This work
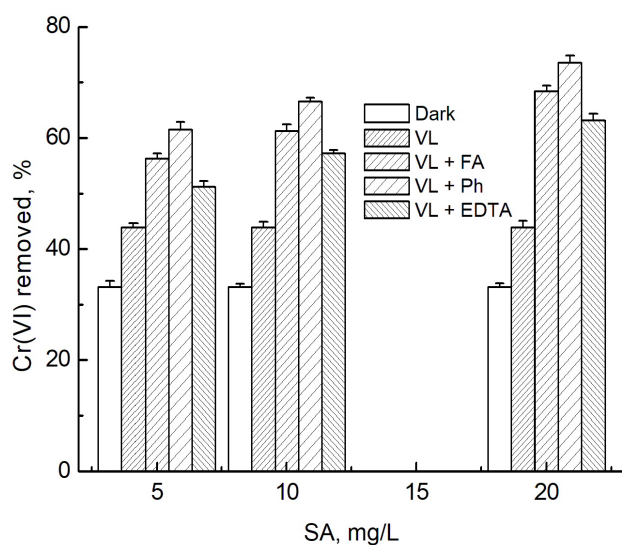
Fig, 9. Effect of different sacrificial agents on Cr(VI) photoreduction using Mn-MNP-3 catalyst ([Cr(VI)], 20 mg/L; pH, ~ 5.0; reaction time, 4 h).

In the presence of sacrificial electron donor, the photogenerated holes (h^+) are quickly consumed to inhibit the recombination of electron-hole pair on the catalyst surface resulting an increase of Cr(VI) reduction by the photogenerated electrons. Besides the above direct pathways, highly reducing aqueous organic radical species, produced by addition of hole (h^+) or $HO^{\check{y}}$ (Eqns. (3) and (5)) with SA, can also take part in reduction of Cr(VI) to Cr(III) [49].

3.2.3. Simultaneous remediation of Cr(VI) and dye

The textile and leather industry wastewaters often contain significant amount of heavy metal pollutants (e.g. Cr^{VI}) along with organic dyes. In this regard, photocatalytic systems capable of removal of both Cr(VI) and dye simultaneously would be beneficial in real system application. In order to see the efficiency of present photocatalysts, simulated mixture solutions containing varying concentrations of Cr(VI) and Congo red (CR) were treated with visible light irradiation under similar conditions used in the case of single component. The results obtained with and without visible light irradiation, are presented in Table 4. In presence of CR, the percentage of Cr(VI) reduction under visible light irradiation is higher than that observed with Cr(VI) alone. Also at a particular concentration, Cr(VI) reduction increases with increase of CR concentration from 10 to 30 mg/L. Similarly the decolourisation of CR is relatively higher in presence of Cr(VI) than that obtained when treated alone. Increase of both Cr(VI) reduction and CR decolourisation is attributed to their synergistic effect in the binary system. In this process, CR acts a scavenger for the photogenerated holes in the catalyst like other sacrificial agents and suppresses the hole-electron recombination to facilitate the Cr(VI) reduction by using the readily available photogenerated electrons. Similarly Cr(VI) acts as an electron scavenger to suppress the recombination of electron-hole pairs and enhance the oxidation of CR using the photogenerated holes. Enhanced photoactivity in binary systems due to cooperative photocatalytic reduction of Cr(VI) and oxidation of dye utilizing the photogenerated electrons and holes simultaneously has been reported in the other photocatalysts [16–19,48]. More studies with wide variation of Cr(VI) and CR concentration ratios are needed to optimize the condition for maximal synergistic effect.

Table 4
Simultaneous photocatalytic reduction of Cr(VI) and decolourisation of Congo red using Mn-MNP-3 (Reaction time, 4 h; pH ~ 5.0)

[Cr(VI)], mg/L	[CR], mg/L	Cr(VI) reduced, %	CR decolourised, %
5.0	–	84.5 (69.0)	–
10.0	–	67.6 (57.2)	–
20.0	–	43.9 (33.4)	–
–	10.0	–	99.5 (49.3)
–	20.0	–	95.3 (26.5)
–	30.0	–	74.3 (19.2)
10.0	10.0	69.6 (30.9)	98.7 (42.7)
10.0	20.0	79.9 (28.5)	97.5 (22.5)
10.0	30.0	88.3 (23.4)	79.3 (16.2)
20.0	10.0	55.3 (24.3)	99.07 (43.4)
20.0	30.0	59.1 (21.5)	81.3 (16.2)

*Values inside the parentheses are without visible light irradiation

4.. Conclusions

Single phase nanometric Mn(II) substituted magnetite samples, ($Mn_xFe_{3-x}O_4$; $0.0 \leq x \leq 0.63$) were prepared by coprecipitation and characterised by various physical methods. XRD data confirmed the cubic spinel structure of all the samples. All the samples showed super paramagnetic behaviour at room temperature with relatively lower saturation magnetization (σ_s) values than bulk magnetite which varied significantly with Mn(II) content in the samples. The band gap values (E_g) decreased from 1.65 to 1.53 eV with increase of Mn(II) substitution. The photocatalytic efficiency of as synthesized samples were tested for decolourisation of different organic dyes and reduction of Cr(VI) to Cr(III) under visible light irradiation. Mn-MNP-3 (x = 0.205) showed the highest activity among all towards photo-decolourisation of dyes; the activity decreased on further increase of Mn^{2+} content. Addition of different sacrificial agents like formic acid, phenol, EDTA showed significant increase of Cr(VI) reduction. Furthermore, Mn-MNP-3 also proved efficient for simultaneous reduction of Cr(VI) to Cr(III) and decolourisation of a dye (Congo red). Simultaneous decontamination of Cr(VI) and dye may find application in treatment of textile wastewater containing both residual dye and heavy metals like Cr(VI).

References

[1] Klaus Hunger, Industrial Dyes – Chemistry, Properties, Application, Wiley, 2003.
[2] H. Zollinger, Color Chemistry: Synthesis, properties and applications of organic dyes and pigments, VCH Publishers, New York, NY, USA, 1987.
[3] M.T. Yagub, T.K. Sen, S. Afroze, H.M. Ang, Dye and its removal from aqueous solution by adsorption: A review, Adv. Colloid Interf. Sci., 209 (2014) 172–184.
[4] Y. Anjaneyulu, N.S. Chary, D.S. Suman Raj, Decolourization of industrial effluents–available methods and emerging technologies—a review, Rev. Environ. Sci. Biotechnol., 4 (2005) 245–273.
[5] N.M. Julkapli, S. Bagheri, S.B.A. Hamid, Recent advances in heterogeneous photocatalytic decolorization of synthetic dyes, Scient. World J. 2014, http://dx.doi.org/10.1155/2014/692307.
[6] V.M. Correia, T. Stephenson, S.J. Judd, Characterization of textile wastewaters—a review, Environ. Technol., 15 (1994) 917–929.
[7] M. Owlad, M.K. Aroua, W.A.W. Daud, S. Baroutian, Removal of hexavalent chromium-contaminated water and wastewater: A review, Water Air Soil Pollut., 200 (2009) 59–77.
[8] Guidelines for Drinking-Water Quality, 4th ed., World Health Organisation, 2011.
[9] E. Forgacs, T. Cserhati, G. Oros, Removal of synthetic dyes from waste waters: a review, Environ. Int., 30 (2004) 953–971.
[10] F. Fu, Q. Wang, Removal of heavy metal ions from wastewaters: a review, J. Environ. Manage., 92 (2011) 407–418.
[11] A. Kumar, C. Guo, G. Sharma, D. Pathania, Mu Naushad, S. Kalia, P. Dhiman, Magnetically recoverable $ZrO_2/Fe_3O_4/$ Chitosan nanomaterials for enhanced sunlight driven photoreduction of carcinogenic Cr(VI) and dechlorination and mineralization of 4-chlorophenol from simulated waste water, RSC Adv., 6 (2016) 13251–13263.
[12] C.C. Chen, W.H. Ma, J.C. Zhao, Semiconductor-mediated photodegradation of pollutants under visible-light irradiation, Chem. Soc. Rev., 39 (2010) 4206–4219.
[13] D. Yue, X. Qian, Y. Zhao, Photocatalytic remediation of ionic pollutant, Sci. Bull., 60 (2015) 1791–1806.
[14] F. Fresno, R. Portela, S. Suarez, J.M. Coronado, Photocatalytic materials: recent achievements and near future trends, J. Mater. Chem. A, 22 (2014) 863–884.
[15] D. Robert, S. Malato, Solar photocatalysis: a clean process for water detoxification, Sci. Total Environ., 291 (2011) 85–97.
[16] B. Thomas, L.K. Alexander, Enhanced synergetic effect of Cr(VI) ion removal and anionic dye degradation with superparamagnetic cobalt ferrite meso–macroporous nanospheres, Appl. Nanosci., 8 (2018) 125–135.
[17] H. Liu, T. Liu, Z. Zhang, X. Dong, Y. Liu, Z. Zhu, Simultaneous conversion of organic dye and Cr(VI) by SnO_2/rGO microcomposites, J. Mol. Catal. A, 410 (2015) 41–48.
[18] F. Jing, R. Liang, J. Xiong, R. Chen, S. Zhang, Y. Li, L. Wu, MIL-68(Fe) as an efficient visible-light-driven photocatalyst for the treatment of a simulated waste-water contain Cr(VI) and Malachite Green, Appl. Catal. B, 206 (2017) 9–15.
[19] X. Zhao, Q. Li, X. Zhang, H. Su, K. Lan, A. Chen, Simultaneous removal of metal ions and methyl orange by combined selective adsorption and photocatalysis, Environ. Prog. Sustain. Energy, 30 (2011) 567– 575.
[20] N.O.S. Keskin, A. Celebioglu, O.F. Sarioglu, A.D. Ozkan, T. Uyar, T. Tekinay, Removal of a reactive dye and hexavalent chromium by a reusable bacteria attached electrospun nanofibrousm web, RSC Adv., 5 (2015) 86867.
[21] D. Cetin, S. Donmez, G. Donmez, The treatment of textile wastewater including chromium(VI) and reactive dye by sulfate-reducing bacterial enrichment, J. Environ. Manage., 88 (2008) 76–82.
[22] S. Laurent, D. Forge, M. Port, A. Roch, C. Robic, L. Vander Elst, R.N. Muller, Magnetic iron oxide nanoparticles: synthesis, stabilization, vectorization, physicochemical characterizations, and biological applications, Chem. Rev., 108 (2008) 2064–2110.
[23] J. Amighian, E. Karimzadeh, M. Mozaffari, The effect of Mn^{2+} substitution on magnetic properties of $Mn_xFe_{3-x}O_4$ nanoparticles prepared by coprecipitation method, J. Magne. Magn. Mater., 332 (2013) 157–162.
[24] Md. Amir, A. Baykal, S. Güner, H. Güngüneş, H. Sözeri, Magneto optical investigation and hyperfine interactions of copper substituted Fe_3O_4 nanoparticles, Ceram. International, 41 (2015) 231–239.
[25] J. Giri, P. Pradhan, V. Somani, H. Chelawat, S. Chhatre, R. Banerjee, D. Bahadur, Synthesis and characterizations of water-based ferrofluids of substituted ferrites [$Fe_{1-x}B_xFe_2O_4$, B = Mn, Co (x = 0–1)] for biomedical applications, J. Magne. Magn. Mater., 320 (2008) 724–730.
[26] P. Saravanan, S. Alam, L.D. Kandpal, G.N. Mathur, Effect of substitution of Mn ion on magnetic properties of Fe_3O_4 nanocrystallites, J. Mater. Sci. Lett., 21 (2002) 2135–2137.

[27] H.W.P. Carvalho, P. Hammer, S.H. Pulcinelli, C.V. Santilli, E.F. Molina, Improvement of the photocatalytic activity of magnetite by Mn-incorporation, Mater. Sci. Eng. B, 181 (2014) 64–69.

[28] H. Zhu, S. Zhang, Y.-X. Huang, L. Wu, S. Sun, Monodisperse $M_xFe_{3-x}O_4$ (M = Fe, Cu, Co, Mn) nanoparticles and their electrocatalysis for oxygen reduction reaction, Nano Lett., 6 (2013) 2947–2951.

[29] X. Liang, Z. He, G. Wei, P. Liu, Y. Zhong, W. Tan, P. Du, J. Zhu, H. He, J. Zhang, The distinct effects of Mn substitution on the reactivity of magnetite in heterogeneous Fenton reaction and Pb(II) adsorption, J. Colloid Interf. Sci., 426 (2014) 181–189.

[30] E. Casbeer, V.K. Sharma, X.-Z. Li, Synthesis and photocatalytic activity of ferrites under visible light: A review, Sep. Purif. Technol., 87 (2012) 1–14.

[31] J. Zhu, S. Wei, M. Chen, H. Gu, S.B. Rapole, S. Pallavkar, T.C. Ho, J. Hopper, Z. Guo, Magnetic nanocomposites for environmental remediation, Adv. Powder Technol., 24 (2013) 459–467.

[32] A.A. Alqadami, Mu Naushad, M.A. Abdalla, M.R. Khan, Z.A. Alothman, Adsorptive removal of toxic dye using Fe_3O_4–TSC nanocomposite: Equilibrium, kinetic, and thermodynamic studies, J. Chem. Eng. Data, 61(11) (2016) 3806–3813.

[33] P.K. Boruah, P. Borthakur, G. Darabdhara, C.K. Kamaja, I. Karbhal, M.V. Shelke, P. Phukan, D. Saikia, M.R. Das, Sunlight assisted degradation of dye molecules and reduction of toxic Cr(VI) in aqueous medium using magnetically recoverable Fe_3O_4/reduced graphene oxide nanocomposite, RSC Adv., 6 (2016) 11049–11063.

[34] S.K. Giri, N.N. Das, G.C. Pradhan, Synthesis and characterization of magnetite nanoparticles using waste iron ore tailings for adsorptive removal of dyes from aqueous solution, Colloid Surf. A, 389 (2011) 43–49.

[35] JCPDS-Joint Committee on Powder Diffraction Standards 26, 1997.

[36] J. Wang, G. Liu, Y. Liu, C. Zhou, Y. Wu, Photocatalytic degradation of methyl orange by Fe_2O_3-Fe_3O_4 nanoparticles and Fe_2O_3-Fe_3O_4-montmorillonite nanocomposites, Clean – Soil Air Water, 45 (2017) 1600472.

[37] Q. Feng, S. Li, W. Ma, H.-J. Fan, X. Wan, Y. Lei, Z. Chen, J. Yang, B. Qin, Synthesis and characterization of Fe_3O_4/ZnO-GO nanocomposites with improved photocatalytic degradation methyl orange under visible light irradiation, J. Alloys Compd., 737 (2018) 197–206.

[38] R.V. Solomon, I.S. Lydia, J.P. Merlin, P. Venuvanalingam, Enhanced photocatalytic degradation of azo dyes using nano Fe_3O_4, J. Iranian Chem. Soc., 9 (2012) 101–109.

[39] S. Bharati, D. Nataraj, D. Mangalraj, Y. Masuda, K. Senthil, K. Yong, Highly mesoporous α-Fe_2O_3 nanostructures: preparation, characterization and improved photocatalytic performance towards Rhodamine B (RhB), J. Phys. D: Appl. Phys., 43 (2010) 015501.

[40] S.K. Giri, N. Das, Visible light induced photocatalytic decolourisation of rhodamine B by magnetite nanoparticles synthesised using recovered iron from waste iron ore tailings, Desal. Water Treat., 57 (2016) 900–907.

[41] P. Yuan, D. Liu, M. Fan, D. Yang, R. Zhu, F. Ge, J. Zhu, H. He, Removal of hexavalent chromium [Cr(VI)] from aqueous solutions by the diatomite-supported/unsupported magnetite nanoparticles, J. Hazard. Mater., 173 (2010) 614–621.

[42] N. Sezgin, A. Yalçın, Y. Köseoğlu, $MnFe_2O_4$ nano spinels as potential sorbent for adsorption of chromium from industrial wastewater, Desal. Water Treat., 57 (2016) 16495–16506.

[43] J. Hu, I.M.C. Lo, G. Chen, Comparative study of various magnetic nanoparticles for Cr(VI) removal, Sep. Purific. Technol., 56 (2007) 249–256.

[44] L. Yang, F. Wang, Y.-F. Meng, Q.-H. Tang, Z-Q. Liu, Fabrication and characterization of manganese ferrite nanospheres as a magnetic adsorbent of chromium, J. Nanomater., 2013 (2013) 1–5.

[45] G. Ren, X. Wang, P. Huang, B. Zhong, Z. Zhang, L. Yang, X. Yang, Chromium(VI) adsorption from wastewater using porous magnetite nanoparticles prepared from titanium residue by a novel solid phase reduction method, Sci. Total Environ., 607–608 (2017) 900–910.

[46] M.R. Lasheen, I.Y. El-Sherif, D.Y. Sabry, S.T. El-Wakeel, M.F. El-Shahat, Removal and recovery of Cr(VI) by magnetite nanoparticles, Desal. Water Treat., 52 (2014) 6464–6473.

[47] S. Rajput, C.U. Pittman, D. Mohan, Magnetic magnetite (Fe_3O_4) nanoparticle synthesis and applications for lead (Pb^{2+}) and chromium (Cr^{6+}) removal from water, J. Colloid Interf. Sci., 468 (2015) 334–346.

[48] S. Patnaik, K.K. Das, A. Mohanty, K.M. Parida, Enhanced photo catalytic reduction of Cr (VI) over polymer-sensitized g-C_3N_4/$ZnFe_2O_4$ and its synergism with phenol oxidation under visible light irradiation, Catal. Today, 315 (2018) 52–56.

[49] I.O. Ali, A.G. Mostafa, Photocatalytic reduction of chromate oxyanions on $MMnFe_2O_4$ (M=Zn, Cd) nanoparticles, Mater. Sci. Semiconduct. Process, 33 (2015) 189–198.

[50] C.M. Ma, Y.S. Shen, P.H. Lin, Photoreduction of Cr(VI) ions in aqueous solutions by UV/TiO_2 photocatalytic processes, Int. J. Photoenergy, 10 (2012), 1155–381971.
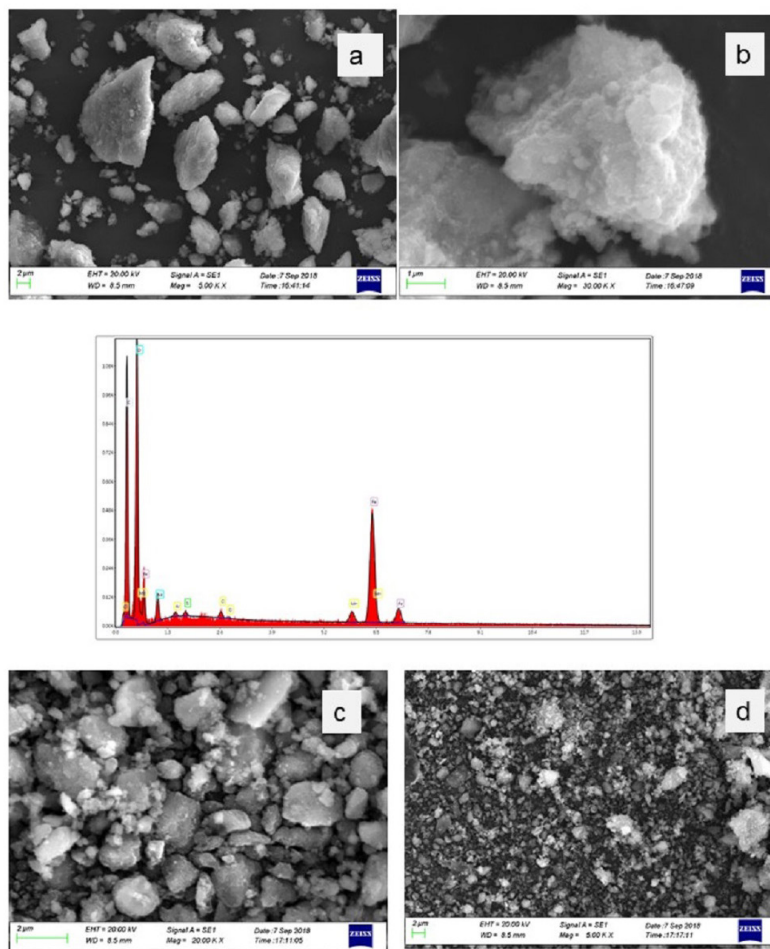
Supplementary

Fig. S1. SEM micrographs of Fe$_3$O$_4$ and Mn-substituted Fe$_3$O$_4$ (Mn-MNP-3). (a, b) Fe$_3$O$_4$, (c, d) Mn-MNP-3.
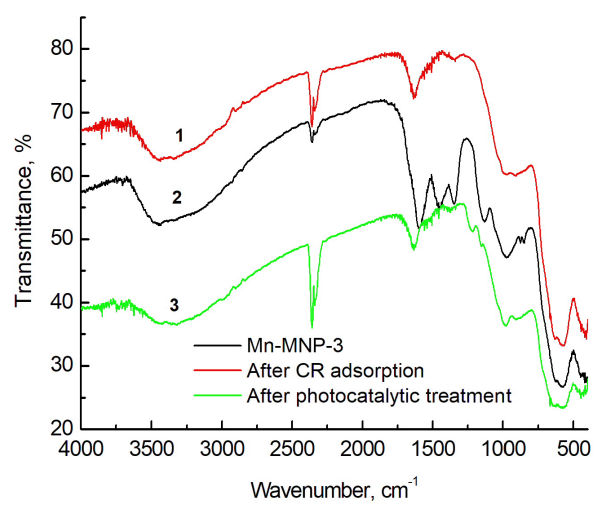

Fig. S2. FT-IR spectra of Mn-MNP-3. (a) neat, (b) after adsorption of CR, and (c) after photocatalytic decolourisation.